



Metal oxide-triazole hybrids as heterogeneous or reaction-induced self-separating catalysts



Tatiana R. Amarante¹, Patrícia Neves¹, Anabela A. Valente*, Filipe A. Almeida Paz*, Martyn Pillinger, Isabel S. Gonçalves*

Department of Chemistry, CICECO – Aveiro Institute of Materials, University of Aveiro, Campus Universitário de Santiago, 3810-193 Aveiro, Portugal

ARTICLE INFO

Article history:

Received 26 April 2016

Revised 3 June 2016

Accepted 4 June 2016

Keywords:

Organic–inorganic hybrid materials

Molybdenum oxide

Catalytic oxidations

Hydrogen peroxide

Catalyst self-separation

ABSTRACT

The hybrid metal oxide-triazole materials [MoO₃(trz)_{0.5}] (**1**) and [W₂O₆(trz)] (**2**) (trz = 1,2,4-triazole) have been hydrothermally synthesized and characterized by different techniques (TGA, SEM, ¹H and ¹³C MAS NMR, FT-IR spectroscopy, and structure determination by Rietveld analysis of high resolution synchrotron powder XRD data). Materials **1** and **2** display distinct behaviors when applied as catalysts for oxidation reactions with alcohol, aldehyde, olefin and sulfide substrates, and are more effective with hydrogen peroxide as the oxidant than with *tert*-butylhydroperoxide. The Mo^{VI} hybrid **1** transforms into soluble active species during *cis*-cyclooctene epoxidation with H₂O₂. When consumption of H₂O₂ reaches completion, spontaneous reassembly of the 2-dimensional molybdenum oxide network of **1** takes place and the hybrid precipitates as a microcrystalline solid that can be easily separated and recycled. Reaction-induced self-separation behavior occurs with **1**, H₂O₂ and other substrates such as methyl oleate and methylphenylsulfide. The W^{VI} hybrid **2** behaves differently, preserving its structural features throughout the heterogeneous catalytic process.

© 2016 Elsevier Inc. All rights reserved.

1. Introduction

An important goal in transition metal catalysis science is the development of systems that combine the advantages of homogeneous catalysts (high activities and selectivities, absence of diffusion limitations, ability to fine-tune performance through ligand modification) with those of heterogeneous catalysts (ease of catalyst-product separation and catalyst recycling) [1,2]. The principal approach to solving this problem has been the immobilization of molecular catalysts onto organic, inorganic or hybrid organic–inorganic supports [3–6]. However, the resultant materials suffer from a number of drawbacks, which include catalyst “leaching”, leading to deactivation, and poor accessibility of the active sites for the substrate. In the period 2001–2003 two papers reported on a new approach involving catalyst self-separation or self-precipitation. The first report, by Xi et al., described reaction-controlled phase-transfer catalysis for propylene oxidation to propylene oxide [7]. The insoluble W-based catalyst precursor formed a soluble active species by the action of H₂O₂. Exhaustion

of the oxidant led to spontaneous precipitation of the catalyst which could be recovered and used again. Later, Dioumaev and Bullock developed an alternative solid–liquid–solid phase separation procedure (for the solvent-free hydrosilylation of carbonyl compounds) that relied on differences in solubility of the catalyst in the liquid substrate and product [8]. The tungsten carbonyl catalyst was initially soluble in the polar substrate but then precipitated upon complete conversion of the substrate and formation of the non-polar liquid product. Since the publication of these two landmark papers, progress on self-precipitating transition metal catalysts has been slow. With some exceptions, such as a redox-switchable phase-tagged ruthenium-based catalyst [9], the solid–liquid–solid phase separation procedures are either reaction-controlled [10–20] or thermoregulated [21–24], and involve polyoxometalate salts of large organic cations [25].

In the present work, we describe a new type of self-separating catalyst based on a molybdenum oxide hybrid material. The material [MoO₃(trz)_{0.5}] (trz = 1,2,4-triazole), which was first reported by Zubieta and co-workers [26], was chosen for study as part of our ongoing investigations into the catalytic properties of molybdenum(VI) and tungsten(VI) oxide-organonitrogen hybrid materials [27–32]. Depending on the structure and composition of these hybrids, as well as the catalytic reaction conditions, the materials typically act either as sources of soluble active species or (more

* Corresponding authors.

E-mail addresses: atav@ua.pt (A.A. Valente), filipe.paz@ua.pt (F.A. Almeida Paz), igoncalves@ua.pt (I.S. Gonçalves).

¹ These authors contributed equally to this work.

rarely) as heterogeneous catalysts. For example, when the materials $[\text{Mo}_2\text{O}_6(2\text{-}(1\text{-pentyl-3-pyrazolyl)pyridine})]$ [30], $[\text{Mo}_3\text{O}_9(2\text{-}[3(5\text{-pyrazolyl})\text{pyridine}])]$ [31] and $[\text{Mo}_3(2,2'\text{-bipy})]$ ($M = \text{Mo}, \text{W}$; $2,2'\text{-bipy} = 2,2'\text{-bipyridine}$) [32] are used in catalytic olefin epoxidation with either *tert*-butylhydroperoxide (TBHP) or hydrogen peroxide as oxidant, they are irreversibly converted into soluble oxodiperoxo complexes of the type $[\text{MO}(\text{O}_2)_2(\text{L})]$, which are responsible for the homogeneous catalytic reaction of the olefin. The efficient recovery and reuse of these complexes is not trivial, typically requiring precipitation with organic solvents. Herein, we describe an unprecedented behavior for the hybrid material $[\text{MoO}_3(\text{trz})_{0.5}]$ when used in catalytic olefin epoxidation with H_2O_2 as oxidant. In a manner similar to that reported with polyoxometalate salts [7,10–20] a solid–liquid–solid phase transfer takes place, with spontaneous reassembly and self-precipitation of the original molybdenum oxide–triazole solid upon completion of the reaction. Results with the molybdenum(VI) hybrid are compared with those for the corresponding tungsten (VI) compound, and the catalytic performances of both materials have been further examined for the oxidation of benzyl alcohol and benzaldehyde. The crystal structures of both hybrids have been determined through Rietveld analysis of high-resolution synchrotron X-ray diffraction data.

2. Experimental

2.1. Materials and methods

For synthesis, MoO_3 (Analar, BDH Chemicals, 99.5%), H_2WO_4 (puriss p.a., Fluka), 1,2,4-triazole (98%, Sigma–Aldrich), and diethyl ether (puriss p.a., Sigma–Aldrich) were acquired from commercial sources and used as received. For the catalytic experiments, the substrates *cis*-cyclooctene (95%), anhydrous benzyl alcohol (99.8%), benzaldehyde ($\geq 99\%$), cyclohexene (99%), *trans*-2-octene (97%), *DL*-limonene ($\geq 95\%$), methyl oleate (99%), methylphenylsulfide (99%) and benzothiophene (95%) were obtained from Sigma–Aldrich and used as received. Acetonitrile (99.9%, Panreac), ethanol (99.9%, Carlo Erba), ethyl acetate (99.9%, Sigma–Aldrich), 5.5 M *tert*-butylhydroperoxide in decane (Sigma–Aldrich), 70 wt.% aq. *tert*-butylhydroperoxide (Sigma–Aldrich), and 30% aq. H_2O_2 (Sigma–Aldrich) were acquired from commercial sources and used as received.

Elemental analysis for C, H, and N was performed at the University of Aveiro with a Leco TruSpec 630–200–200 analyzer. Routine powder X-ray diffraction (PXRD) data were collected at ambient temperature on a Philips Analytical Empyrean ($\theta/2\theta$) diffractometer equipped with a PIXcel1D detector, with automatic data acquisition (X'Pert Data Collector software v4.2) using monochromatized Cu $K\alpha$ radiation ($\lambda = 1.5406 \text{ \AA}$). Intensity data were collected by the step-counting method (step 0.01°), in continuous mode, in the $ca. 5 \leq 2\theta \leq 50^\circ$ range. Scanning electron microscopy (SEM) images were collected using a Hitachi S4100 microscope operating at 25 kV. Samples were prepared by deposition on aluminum sample holders followed by carbon coating using an Emitech K 950 carbon evaporator. Thermogravimetric analysis (TGA) was carried out using a Shimadzu TGA-50 instrument, from ambient temperature to *ca.* 800°C , under a continuous stream of air at a flow rate of 20 mL min^{-1} , and a heating rate of 5°C min^{-1} .

FT-IR spectra were collected using KBr (Sigma–Aldrich, 99%, FT-IR grade) pellets and a Mattson-7000 infrared spectrophotometer. Attenuated total reflectance (ATR) FT-IR spectra were measured using a Specac Golden Gate Mk II ATR accessory having a diamond top plate and KRS-5 focusing lenses. Solid state ^{13}C cross-polarization (CP) magic-angle-spinning (MAS) NMR spectra were

recorded using a Bruker Avance 400 spectrometer (9.4 T) at 100.62 MHz with $3.25 \mu\text{s}$ ^1H 90° pulses, 2 ms contact time, spinning rates of 10–12 kHz, and 3–4 s recycle delays. Chemical shifts are quoted in parts per million (ppm) from tetramethylsilane.

2.2. $[\text{MoO}_3(\text{trz})_{0.5}]$ (**1**)

A mixture of MoO_3 (0.14 g, 0.97 mmol), 1,2,4-triazole (0.05 g, 0.72 mmol) and water (15 mL) was heated in a rotating (15 rpm) Teflon-lined stainless steel digestion bomb at 180°C for 1 h. After cooling down to ambient temperature, the resultant bluish white microcrystalline solid was separated from the aqueous liquor by filtration, washed with an excess of water and diethyl ether ($4 \times 10 \text{ mL}$), and finally dried at ambient temperature. Yield: 0.14 g, 83% (based on Mo). Anal. Calcd for $\text{CH}_{1.5}\text{N}_{1.5}\text{O}_3\text{Mo}$: C, 6.73; H, 0.85; N, 11.77. Found: C, 6.65; H, 1.13; N, 11.73. FT-IR (KBr, cm^{-1}): $\nu = 329$ (m), 374 (s), 437 (m), 595 (vs, br), 626 (sh), 842 (vs, br), 937 (s), 964 (m), 1000 (m), 1058 (m), 1141 (m), 1176 (w), 1222 (w), 1253 (w), 1307 (m), 1425 (m), 1519 (m), 1779 (m), 2300–3000 (several weak bands due to trz), 3116 (s). $^{13}\text{C}\{^1\text{H}\}$ CP MAS NMR: $\delta = 145.8$ ppm.

2.3. $[\text{W}_2\text{O}_6(\text{trz})]$ (**2**)

A mixture of H_2WO_4 (0.49 g, 1.96 mmol), 1,2,4-triazole (0.20 g, 2.90 mmol) and water (25 mL) was heated in a rotating (15 rpm) Teflon-lined stainless steel digestion bomb at 180°C for 93 h. After cooling down to ambient temperature, the resultant yellowish white microcrystalline solid was separated from the aqueous liquor by filtration, washed with an excess of water and diethyl ether ($4 \times 10 \text{ mL}$), and finally dried at ambient temperature. Yield: 0.46 g, 89% (based on W). Anal. Calcd for $\text{C}_2\text{H}_3\text{N}_3\text{O}_6\text{W}_2$: C, 4.51; H, 0.57; N, 7.89. Found: C, 4.45; H, 0.55; N, 7.97. FT-IR (KBr, cm^{-1}): $\nu = 306$ (vs), 372 (m), 406 (w), 426 (w), 447 (w), 622 (s), 684 (sh, br), 732 (vs, br), 906 (s, br), 950 (m), 975 (m), 1002 (w), 1062 (m), 1145 (w), 1226 (w), 1247 (w), 1263 (w), 1311 (m), 1427 (m), 1513 (m), 1521 (m), 1533 (w), 1789 (w), 2500–3000 (several weak bands due to trz), 3106 (s), 3436 (m, br). $^{13}\text{C}\{^1\text{H}\}$ CP MAS NMR: $\delta = 145.1$ ppm.

2.4. Synchrotron powder X-ray diffraction studies

High-resolution synchrotron PXRD data for **1** and **2** were collected at low temperature (100 K; cooling device from Oxford Instruments) on the powder diffractometer assembled at ID22 [33] at the European Synchrotron Radiation Facility (ESRF), Grenoble, France. The beam line receives X-rays from the synchrotron source, operating with an average energy of 6 GeV and a beam current of typically 200 mA, from an undulator device. The high signal-to-noise ratio of the data is due to the high brilliance of the synchrotron beam in combination with a Si(111) crystal multi-analyzer.

The monochromatic wavelength was fixed at $0.495958(7) \text{ \AA}$ and calibrated against the Si standard NIST 640c [certified cell parameter $a = 5.4311946(92) \text{ \AA}$]. Hard X-rays were selected for data collection in order to significantly reduce radiation damage, an occurrence observed in previous investigations using related materials but under different experimental conditions [27,29,31]. Even at low temperature the high brilliance of the synchrotron source led to visible damage of the samples. To minimize such effects consecutive data collections were performed on fresh portions of the samples by translating the capillaries by *ca.* 1.3 mm.

Finely powdered samples of compounds **1** and **2** were placed inside a Hilgenberg borosilicate glass capillary (*ca.* 0.9 mm in diameter) which was spun during data collection to improve powder averaging over the individual crystallites, ultimately removing

textural effects such as preferred orientation. Data were collected in continuous mode with accumulation times increasing with the scattering angle. The counts of the six detectors (covering roughly $5.5^\circ 2\theta$) were rebinned and normalized to give the equivalent step scans (0.002°) suitable for further structural analyses.

The collected high-resolution PXRD patterns were indexed using the LSI-Index algorithm implemented in TOPAS-Academic V5 [34,35] and a whole-powder-pattern Pawley fit allowed the orthorhombic space groups *Pbcm* and *P2₁2₁2₁* to be unequivocally confirmed as the most suitable for compounds **1** and **2**, respectively. Pattern indexation and symmetry search permitted, on the one hand, to identify **1** as isotypical with that reported by Hagrman et al. [26], despite the presence of a residual amount of an unidentified crystalline impurity (ten excluded zones in Fig. 1). On the other hand, this initial procedure revealed that the replacement of Mo^{VI} by W^{VI} (to isolate **2**) induced some modifications on the local symmetry elements of the compound. In bulk **2**, a residual amount of an unidentified impurity could also be observed as indicated by the single excluded region in Fig. 2.

The two crystal structures were determined in TOPAS-Academic V5 [34] by using a simulated annealing approach. The adopted strategy combined the use of individual chemical moieties for the crystallographically independent metal centers (Mo and W) and individual (terminal and bridging) oxygen atoms, and also the use of Fenske–Hall Z-matrices for the *N,N*-bridging organic linkers. This complex strategy greatly facilitates the mobility of all chemical entities inside the unit cell boundaries during the global optimization processes, while also allowing the inclusion of various antibump and distance restraints for the optimization procedures.

Rietveld structural refinements were performed with TOPAS-Academic V5 [34] using a Chebyshev polynomial throughout the entire angular range to model the background contribution. The peak shapes for the powder pattern were described using the fundamental parameters approach [36], with preferred orientation effects being modeled using either a 4th or 8th order spherical harmonics approach, for **1** and **2** respectively. The final Rietveld refinement was performed considering the presence of crystalline impurity phases contributing to both powder patterns: a total of ten (for **1**) and one (for **2**) excluded zones were included in the final models (see Figs. 1 and 2 for additional details).

Table S1 in the Supplementary Material gathers all the details pertaining to the ID22 high-resolution synchrotron PXRD data collection, crystal data and structure refinement details for compounds **1** and **2**. CCDC 1436239 (**1**) and 1436238 (**2**) contain the supplementary crystallographic data for this paper. These data can be obtained free of charge from The Cambridge Crystallographic Data Centre via <https://summary.ccdc.cam.ac.uk/structure-summary-form>.

2.5. Catalytic tests

Catalytic reactions were carried out at 70 °C in 5 mL borosilicate reactors equipped with valves for sampling and a PTFE magnetic stirring bar. Typically, an amount of hybrid compound equivalent to 18 μmol of Mo or W, 1.8 mmol of substrate (1.2 M), and 1 mL of cosolvent (CH₃CN) was added to the reactor, which was then immersed in a temperature-controlled oil bath. After stirring (1000 rpm) for 10 min, oxidant (2.75 mmol) was added, and the reaction time was counted from this instant.

The evolution of the catalytic reactions was monitored by gas chromatography (GC). Individual experiments were performed for a given reaction time; prior to sampling, the reactors were cooled to ambient temperature. The samples were analyzed using a Varian 3900 GC equipped with a DB-5 capillary column (30 m × 0.25 mm × 0.25 μm) and a FID detector, with H₂ as the

carrier gas. The identification of the reaction products was carried out by GC–MS (GC–qMS Agilent Technologies, 6890 N Network GC system, 5973 Network mass selective detector, equipped with a DB-1 capillary column (30 m × 0.25 mm × 0.10 μm)), using He as the carrier gas.

After a 24 h batch run of *cis*-cyclooctene (Cy) epoxidation, the solid was separated from the reaction mixture by centrifugation (3500 rpm), thoroughly washed with pentane or ethanol, and vacuum-dried at 60 °C for 1 h. The recovered solid was reused twice for Cy epoxidation under typical conditions (the initial mass ratios of olefin:oxidant:metal compound were the same for all runs).

Contact tests (ct) were carried out for **1** and **2** as follows. The compound was treated with oxidant (H₂O₂) and solvent (CH₃CN) under similar conditions to those used for a typical batch run, but without substrate, for 24 h at 70 °C. Subsequently, the mixture was cooled to ambient temperature and centrifuged (3500 rpm). The liquid phase (L) was passed through a filter equipped with a 0.2 μm nylon membrane (giving **1**-L-ct and **2**-L-ct for **1** and **2**, respectively), and used for the homogeneous catalytic reaction of Cy with H₂O₂; Cy was added to the liquid to give an initial substrate concentration of 1.2 M, and this solution was stirred for 24 h at 70 °C.

The contact test with **1** led to a yellow solution (**1**-L-ct); partial evaporation of this solution at 70 °C resulted in the precipitation of a yellow solid denoted PS-(**1**-L-ct). The contact test with **2** led to a biphasic solid–liquid mixture; the solid was recovered in a similar fashion to that described above for catalyst reuse, giving **2**-S-ct. The solids PS-(**1**-L-ct) and **2**-S-ct were tested as catalysts for the reaction of Cy with H₂O₂ at 70 °C (the initial olefin:oxidant:metal compound mass ratios were the same as those used under the typical reaction conditions). After 24 h catalytic batch runs with these solids, biphasic solid–liquid mixtures were obtained; the solids were recovered in a similar fashion to that described above for catalyst reuse, giving (PS-(**1**-L-ct))-run1 and (**2**-S-ct)-run1, respectively.

All of the recovered solids obtained in the catalytic and contact tests were characterized by ATR FT-IR spectroscopy and/or PXRD. Selected solids were also studied with SEM.

3. Results and discussion

3.1. Catalyst synthesis and characterization

The molybdenum oxide hybrid [MoO₃(trz)_{0.5}] (**1**) was obtained in very good overall yield by the reaction of MoO₃, 1,2,4-triazole (trz) and H₂O in the mole ratio of ca. 1:0.75:830 at 180 °C for 1 h in a Teflon-lined digestion bomb. Previously, Zubieta and co-workers reported the isolation of **1** as light yellow blocks in 74% yield by the reaction of Na₂MoO₄, trz, NiCl₂, and H₂O in the mole ratio 1:0.95:1.67:1465 at 200 °C for 136 h [26]. In the present work, only a dynamic hydrothermal synthesis (i.e., with continuous rotation of the bomb) led to complete reaction of MoO₃ to give **1**. The corresponding tungsten oxide hybrid, [W₂O₆(trz)] (**2**), which has not been previously reported, was prepared in a similar fashion with 89% yield by heating H₂WO₄, trz, and H₂O in the mole ratio 1:1.5:1400 for 93 h at 180 °C.

TGA for compounds **1** and **2** showed no weight loss up to about 305 °C for **1** and 400 °C for **2** (Fig. S1 in the Supplementary Material). Thermal decomposition of the organic ligand above these temperatures leads to residual masses of 79.9% at 420 °C for **1** and 86.8% at 480 °C for **2**, which are in excellent agreement with the calculated values of 80.6% and 87.0% for the stoichiometric formation of MO₃ (M = Mo, W). Whereas the residual WO₃ undergoes

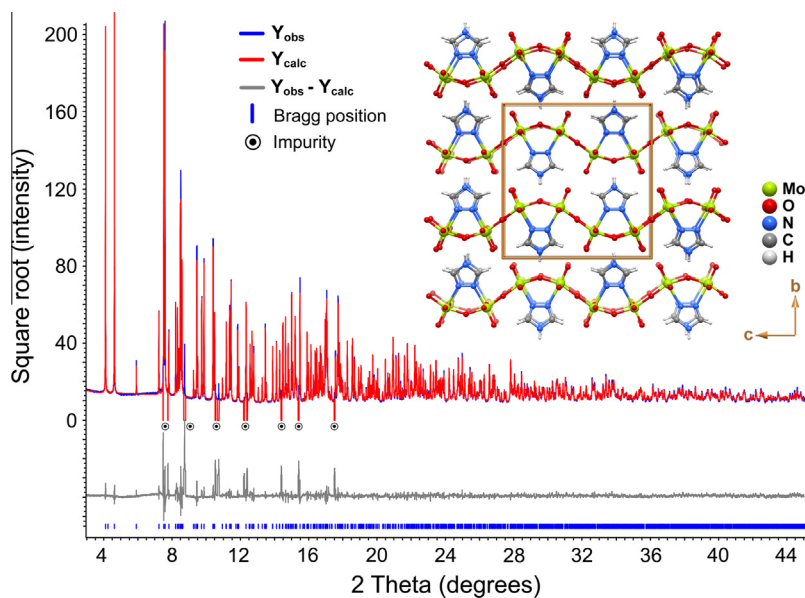


Fig. 1. Final Rietveld plot of $[\text{MoO}_3(\text{trz})_{0.5}]$ (**1**). Observed data points are indicated as a blue line, and the best fit profile (upper trace) and difference pattern (lower trace) are drawn as solid red and gray lines, respectively. Blue vertical bars indicate the angular positions of the allowed Bragg reflections for **1**. Refinement details are given in Table S1 in the Supplementary Material. The inset depicts a perspective view along the $[100]$ direction of the unit cell.

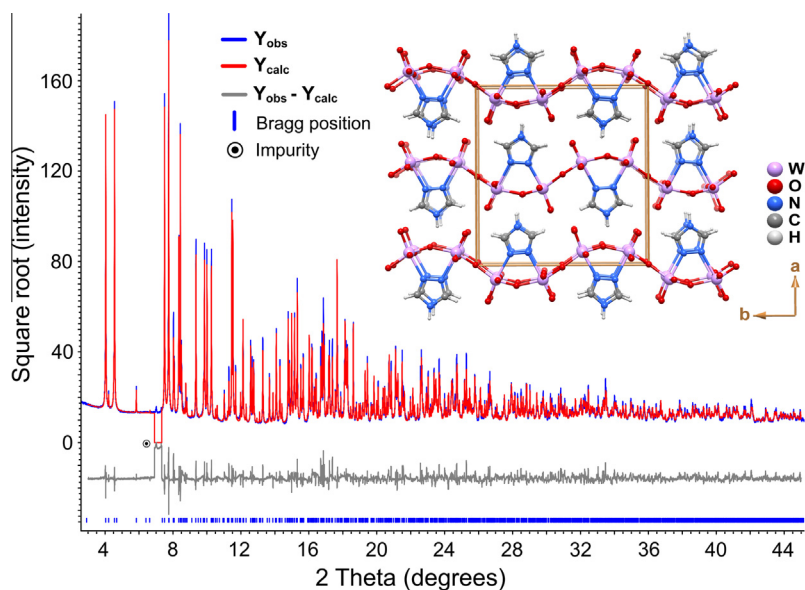


Fig. 2. Final Rietveld plot of $[\text{W}_2\text{O}_6(\text{trz})]$ (**2**). Observed data points are indicated as a blue line, and the best fit profile (upper trace) and difference pattern (lower trace) are drawn as solid red and gray lines. Blue vertical bars indicate the angular positions of the allowed Bragg reflections for **2**. Refinement details are given in Table S1 in the Supplementary Material. The inset depicts a perspective view along the $[001]$ direction of the unit cell.

no further weight loss up to $800\text{ }^\circ\text{C}$, the residual MoO_3 starts to sublime above $700\text{ }^\circ\text{C}$.

SEM of **1** showed that the morphology consists of rectangular blocks with typical widths in the range of $1.5\text{--}2.5\text{ }\mu\text{m}$ and lengths in the range of $5\text{--}9\text{ }\mu\text{m}$ (Fig. 3). By contrast, compound **2** exhibits a needle-like morphology, quite similar to that found recently for $[\text{WO}_3(2,2'\text{-bipyridine})]$ [32].

The FT-IR spectra of **1** and **2** are similar in the range of $1000\text{--}3200\text{ cm}^{-1}$, displaying bands that are attributed mainly to the triazole ligand (Fig. S2 in the Supplementary Material). In particular, we may single out medium-to-strong bands in the $1500\text{--}1540\text{ cm}^{-1}$ range assigned to $\nu(\text{C}=\text{N})$ and a sharp band at about 3110 cm^{-1} assigned to $\nu(\text{CH})$ [37]. An alternative assignment for

the latter band is $\nu(\text{NH})$. Such relatively low frequencies for $\nu(\text{NH})$ are possible when the group is involved in a significant hydrogen bonding interaction [38]. As will be described below, this is the case for **1** (involving an interaction between the $\text{N}\text{--}\text{H}$ group of a triazole of one layer and a bridging oxo group of an adjacent layer), but not for **2**. Therefore the assignment of the sharp band to $\nu(\text{CH})$ seems more plausible. Below 1000 cm^{-1} , the spectra of **1** and **2** display some notable differences. The hybrid **1** exhibits a strong band at 937 cm^{-1} , assigned to $\nu(\text{Mo}=\text{O})$, and two very strong, broad bands at 595 and 842 cm^{-1} , assigned to $\nu(\text{Mo}\text{--}\text{O}\text{--}\text{Mo})$. The corresponding bands for **2** can be tentatively identified as a medium intensity band at 950 cm^{-1} [$\nu(\text{W}=\text{O})$] and a very strong, broad band at 732 cm^{-1} , which has a broad shoulder

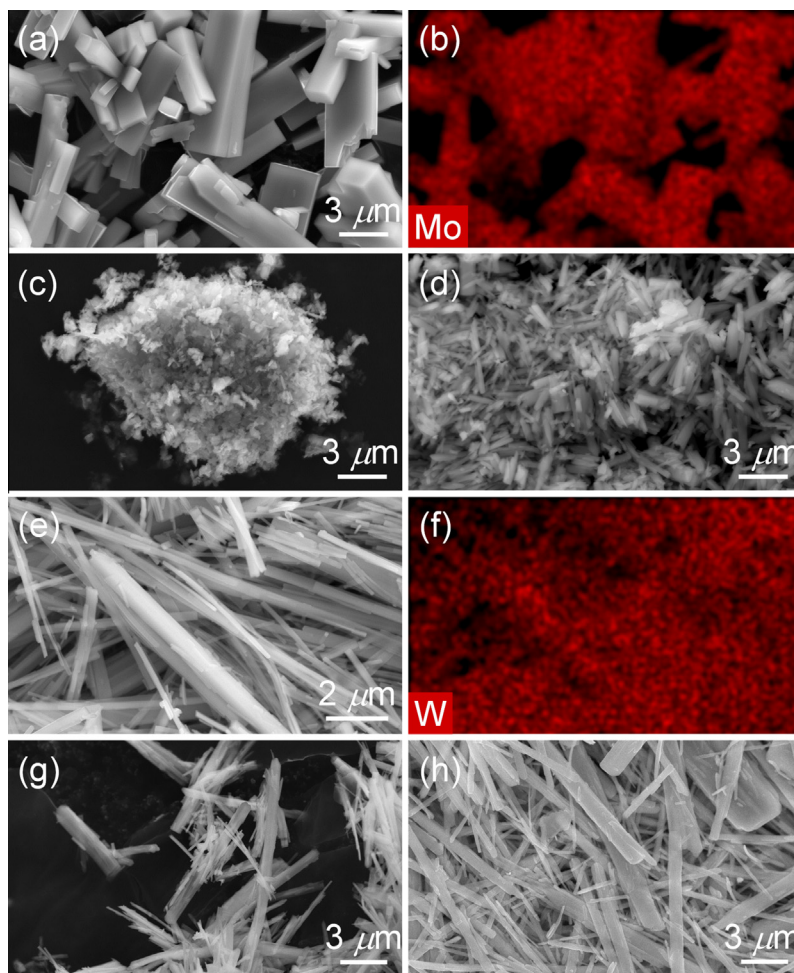


Fig. 3. SEM images of (a) compound **1**, (c) **1**/H₂O₂-run1, (d) PS-(1-L-ct), (e) compound **2**, (g) **2**/H₂O₂-run1, and (h) **2**-S-ct. The EDS elemental distribution maps corresponding to the images (a) and (e) are shown in (b) and (f), respectively.

centered at *ca.* 680 cm⁻¹ [$\nu(\text{W—O—W})$]. Both of the spectra for **1** and **2** display a sharp band at about 625 cm⁻¹ assigned to a triazole ring torsion vibration [39]. In a study of the infrared spectra of several transition metal triazole complexes, Haasnoot et al. concluded that the presence of one ring torsion band in the 600–700 cm⁻¹ range, typically around 630 cm⁻¹, is indicative of 4-H,1,2-coordinating triazole rather than 1-H,2,4-coordinating triazole [39], and therefore the spectra for **1** and **2** are consistent with the presence of metal centers bridged by 1,2-bicoordinating triazole ligands.

The solid-state ¹H and ¹³C{¹H} MAS NMR spectra of **1** and **2** were very similar, which is consistent with both compounds having the same type of topological motif containing bridging trz units. Hence, the ¹³C{¹H} CP MAS NMR spectra display a single sharp resonance in the 145–146 ppm range attributed to the carbon atoms C3 and C5, which are chemically equivalent due to the N1,N2 bridging mode adopted by the ligand (Fig. S3 in the Supplementary Material). The ¹H MAS NMR spectra display one resonance in the 9.6–9.9 ppm range and another in the 13.7–14.6 ppm range assigned to the CH (H3/H5) and NH protons, respectively. An additional signal at 5.1 ppm can be attributed to residual amounts of physisorbed water molecules.

3.2. High-resolution synchrotron PXRD studies

The structures of compounds **1** and **2**, which were isolated as microcrystalline powders, were investigated on the basis of PXRD

data collected at the ESRF (Grenoble, France). As clearly observed in both collected patterns, the materials contain trace amounts of crystalline impurities (Figs. 1 and 2), which remain unidentified to date. None of the impurities correspond to the starting materials used in the synthesis or possible secondary products with crystalline structures deposited in the Cambridge Structural Database.

Topologically, the replacement of Mo^{VI} centers by W^{VI} does not affect the main structural features of the materials, with the most striking motif present in both crystal structures being neutral two-dimensional $\infty[\text{MoO}_3(\text{trz})_{0.5}]$ and $\infty[\text{W}_2\text{O}_6(\text{trz})]$ layers placed in the *ac* and *bc* planes of the respective unit cells (see insets in Figs. 1 and 2). The major differences lie in the small crystallographic details. While **1** is based on a single crystallographically independent Mo center with the asymmetric unit containing only half of one 1,2,4-triazole molecule (the mirror plane of the *Pbcm* space group bisects the organic bridge as depicted in Fig. 4a), the modification of the space group for **2** (while the Laue symmetry remains identical) leads to a different asymmetric unit containing instead two metal centers and an entire organic linker (Fig. 4b). Attempts to model **2** with the same symmetry elements as those found in the Mo-based material failed, clearly indicating that the material has a completely distinct space group (this was true for XRD data collected at both 100 K and at ambient temperature using standard laboratory equipment). We attribute this modification in the space group to the small, but significantly larger, effective ionic radius of hexacoordinated W^{VI} which, ultimately, leads to a distinct crystal

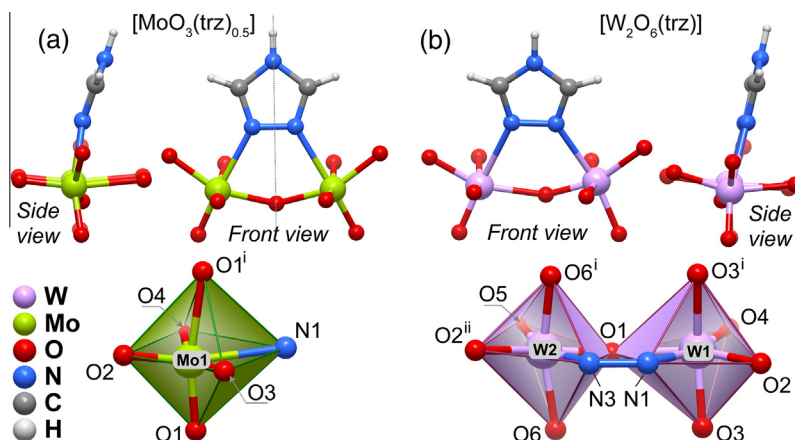


Fig. 4. Schematic representation of portions of the 2D neutral $[\text{MoO}_3(\text{trz})_{0.5}]$ (a) and $[\text{W}_2\text{O}_6(\text{trz})]$ (b) layers present in the crystal structures of **1** and **2**, respectively, emphasizing the crystallographically independent Mo and W coordination environments and the coordination mode of the trz ligand. For **1**, the mirror plane along the *c*-axis bisects the organic ligand (indicated by the dashed gray line); for **2**, the local symmetry is changed with displacement of the organic ligand and increased distortion of the coordination polyhedra. Selected bond lengths and angles are given in Tables 1 and 2. Symmetry transformations used to generate equivalent atoms: For **1**, (i) $-1 + x, y, z$; for **2**, (i) $x, y, -1 + z$, (ii) $1 - x, -\frac{1}{2} + y, 1.5 - z$.

packing. This additional distortion is also clearly noticeable when attention is focussed on the bridging organic linker itself (Fig. 4b): when looking at analogous positions within the neutral layers, in **2** the bridging 1,2,4-triazole is tilted and closer to one metal center.

The coordination environments of all metal centers in **1** and **2** closely resemble distorted octahedra, in which each metal center is bound to four μ_2 -bridging oxo groups, one terminal oxo moiety and one nitrogen atom of the *N,N*-bridging trz ligand. The terminal oxo group appears *trans* coordinated to the organic linker, clearly exerting the well-known *trans* effect and, thus, contributing to the overall distortion of the $\{\text{MoNO}_5\}$ and $\{\text{WNO}_5\}$ octahedra. For **1**, the Mo–(N,O) bond distances range from 1.677(2) to 2.331(3) Å, and the *cis* and *trans* (N,O)–Mo–(N,O) octahedral internal angles are found in the 77.18(9)–104.51(11)° and 154.94(14)–167.21(10)° ranges, respectively (Table 1 and Fig. 4a). These refined values are in very good agreement with the geometrical data reported by Zubietta and co-workers for a single-crystal XRD study of the structure of **1** [26], with the analogous intervals being 1.700(3)–2.354(3) Å, 75.95(15)–104.80(15)° and 153.15(17)–167.26(19)°, respectively. The two crystallographically independent $\{\text{WNO}_5\}$ octahedra present in **2** (W1/W2 – Fig. 4b) have relatively similar coordination environments: the W–(N,O) bond distances were found in the 1.63(2)–2.44(2)/1.692(17)–2.34(3) Å ranges, and the *cis* and *trans* (N,O)–W–(N,O) octahedral angles refined within the 72.7(7)–104.2(8)/76.7(19)–105.2(7)° and 156.0(8)–168.7(9)/158.8(9)–164.9(7)° intervals, respectively (Table 2). As mentioned above, the distinct W1–N and W2–N bond distances are a clear consequence of the local distortion associated with the way the organic ligand bridges neighboring metals.

To help compare these two isotypical materials and to further evaluate a potential variation in the degree of distortion of the metal octahedra between **1** and **2**, we decided to employ an adaptation of the mathematical method proposed by Baur [40] to calculate a distortion index (DI) for bonds and angles:

$$DI_{\text{Bond}} = \frac{\sum_{i=1}^n |d(\text{Metal} - (\text{N}, \text{O}))_i - d(\text{Metal} - (\text{N}, \text{O}))_{\text{average}}|}{\sum_{i=1}^n |d(\text{Metal} - (\text{N}, \text{O}))_i|} \quad (1)$$

$$DI_{\text{Angle}} = \frac{\sum_{i=1}^n |\angle((\text{N}, \text{O}) - \text{Metal} - (\text{N}, \text{O}))_i - \angle((\text{N}, \text{O}) - \text{Metal} - (\text{N}, \text{O}))_{\text{ideal}}|}{\sum_{i=1}^n |\angle((\text{N}, \text{O}) - \text{Metal} - (\text{N}, \text{O}))_i|} \quad (2)$$

Table 1

Selected bond lengths (Å) and angles (degrees) for the crystallographically independent Mo metal center present in $[\text{MoO}_3(\text{trz})_{0.5}]$ (**1**).^a

Mo1–O1	1.739(2)	O1–Mo1–O2	104.51(11)
Mo1–O2	1.677(2)	O1–Mo1–O3	96.57(13)
Mo1–O3	1.9250(13)	O1–Mo1–O4	96.91(13)
Mo1–O4	1.8855(6)	O1–Mo1–N1	90.03(11)
Mo1–O1 ⁱ	2.218(2)	O1–Mo1–O1 ⁱ	167.21(10)
Mo1–N1	2.331(3)	O1 ⁱ –Mo1–O2	88.23(10)
		O1 ⁱ –Mo1–O3	80.65(12)
		O1 ⁱ –Mo1–O4	81.54(12)
		O1 ⁱ –Mo1–N1	77.18(9)
		O2–Mo1–O3	96.43(15)
		O2–Mo1–O4	100.51(9)
		O2–Mo1–N1	164.40(11)
		O3–Mo1–O4	154.94(14)
		O3–Mo1–N1	75.97(14)
		O4–Mo1–N1	82.98(7)

^a Symmetry transformation used to generate equivalent atoms: (i) $-1 + x, y, z$.

Table 2

Selected bond lengths (Å) and angles (degrees) for the two crystallographically independent W metal centers present in $[\text{W}_2\text{O}_6(\text{trz})]$ (**2**).^a

W1–O1	2.090(18)	W2–O1	1.692(17)
W1–O2	1.80(3)	W2–O2 ⁱⁱ	1.99(3)
W1–O3	1.844(15)	W2–O5	1.80(2)
W1–O3 ⁱ	2.046(15)	W2–O6	1.964(15)
W1–O4	1.63(2)	W2–O6 ⁱ	1.874(15)
W1–N1	2.44(2)	W2–N3	2.34(3)
O1–W1–O2	158.3(9)	O1–W2–O2 ⁱⁱ	158.8(9)
O1–W1–O3	90.7(6)	O1–W2–O5	96.3(8)
O1–W1–O3 ⁱ	98.2(6)	O1–W2–O6	75.8(6)
O1–W1–O4	104.2(8)	O1–W2–O6 ⁱ	92.0(6)
O1–W1–N1	74.4(9)	O1–W2–N3	76.7(10)
O2–W1–O3	79.3(8)	O2 ⁱⁱ –W2–O5	104.0(10)
O2–W1–O3 ⁱ	84.4(8)	O2 ⁱⁱ –W2–O6	105.2(7)
O2–W1–O4	96.9(11)	O2 ⁱⁱ –W2–O6 ⁱ	82.9(7)
O2–W1–N1	85.9(12)	O2 ⁱⁱ –W2–N3	82.1(12)
O3–W1–O3 ⁱ	156.0(8)	O5–W2–O6	102.1(9)
O3 ⁱ –W1–N1	72.7(7)	O5–W2–O6 ⁱ	88.0(9)
O3–W1–N1	88.5(7)	O5–W2–N3	163.6(12)
O4–W1–O3	102.8(10)	O6–W2–O6 ⁱ	164.9(7)
O4–W1–O3 ⁱ	96.6(9)	O6–W2–N3	90.7(11)
O4–W1–N1	168.7(9)	O6 ⁱ –W2–N3	77.6(11)

^a Symmetry transformations used to generate equivalent atoms: (i) $x, y, -1 + z$; (ii) $1 - x, -\frac{1}{2} + y, 1.5 - z$.

where the subscripts *i* and *average/ideal* correspond to individual and average/ideal bond lengths and angles (see Tables 1 and 2 for individual data). As in our previous studies using these distortion degrees, the value of DI_{Angle} should be, for an octahedron, calculated independently for the *cis* and *trans* angles. Although the model by Baur [40] suggested that DI_{Angle} should be calculated with respect to the average values observed for the polyhedra, we shall compare instead with the ideal values of an octahedron (i.e., 90° and 180° for the *cis* and *trans* angles, respectively). Having this in mind, the DI_{Bond} values for the Mo^{VI} and W^{VI} (W1/W2) centers are 0.11 and 0.11/0.08, respectively. The corresponding DI_{Angle} values for the *cis/trans* angles are 0.09/0.11, 0.10/0.12 and 0.10/0.11 for Mo1, W1 and W2, respectively. These results clearly demonstrate that, as a whole, the coordination environments of all metal centers belonging to both structures are roughly equally distorted.

The major consequence of the different space groups for **1** and **2** concerns the way the neutral two-dimensional $[\text{MoO}_3(\text{trz})_{0.5}]_{\infty}$ and $[\text{W}_2\text{O}_6(\text{trz})]_{\infty}$ layers close pack in the solid state. While the former pack on top of each other such that a strong and directional N—H...O interplanar hydrogen bond is established between adjacent layers (dashed green lines in Fig. 5a), the molecular geometry of the latter does not permit the existence of such an interaction (Fig. 5b). Indeed, while in **1** the N—H group of the bridging trz points directly to a μ_2 -bridging oxo group of the neighboring layer, in **2** this moiety is instead pointing to the void space in between metal centers, thus not allowing a hydrogen-bonding interaction to be established.

3.3. Catalytic investigations

3.3.1. Epoxidation of *cis*-cyclooctene

Compounds **1** and **2** were tested as (pre)catalysts for the epoxidation of *cis*-cyclooctene (Cy), chosen as a model substrate, at 70 °C using *tert*-butylhydroperoxide or hydrogen peroxide as oxidant, and acetonitrile as cosolvent [41]. The catalytic performances of **1** and **2** strongly depended on the type of oxidant used (Table 3). With TBHP [either aqueous (TBHP_{aq}) or decane (TBHP_{dec}) solutions] as oxidant, the reaction of Cy was sluggish, giving 20–35% and 3–9% conversion for **1** and **2**, respectively, at 24 h reaction, with a selectivity of 100% for cyclooctene oxide (CyO).

The catalytic performances improved considerably when aq. H_2O_2 was used as oxidant instead of TBHP, leading to 98% and 85% conversion for **1** and **2**, respectively, at 24 h reaction, with CyO again being the only product (Table 3, Fig. 6). The catalytic performance of **1**/ H_2O_2 is superior to that reported for different molybdenum-based compounds tested as catalysts under similar Cy reaction conditions. Epoxide yields in the range of 54–81% (100% selectivity) and turnover numbers calculated at 24 h [TON (24 h)] in the range of 54–81 $\text{mol}_{\text{Cy}} \text{mol}_{\text{Mo}}^{-1}$ were obtained for the complexes $[\text{MoO}(\text{O}_2)_2(\text{L})]$ and $[\text{Mo}_2\text{O}_4(\mu\text{-O})\text{Cl}_2(\text{L})_2]$ (L = 2,2'-bipy, 4,4'-di-*tert*-butyl-2,2'-bipyridine), the octanuclear complex $[\text{Mo}_8\text{O}_{24}(4,4'\text{-di-}i\text{-tert-butyl-2,2'-bipyridine})]$, and the hybrid material $\{[\text{MoO}_3(2,2'\text{-bipy})][\text{MoO}_3(\text{H}_2\text{O})]\}_n$ [42]. High catalytic activity was recently reported for the polyoxometalate salt [1-hexyl-3-methylimidazolium]₄Mo₈O₂₆ (98% Cy conversion at 1 h, 60 °C); a relatively high molybdenum loading was used (12 $\text{mol}_{\text{Mo}}\%$, compared to 1 $\text{mol}_{\text{Mo}}\%$ in the present work), which led to a turnover frequency calculated at 1 h [TOF(1 h)] of 8 $\text{mol}_{\text{Cy}} \text{mol}_{\text{Mo}}^{-1} \text{h}^{-1}$ (for **1**, TOF(1 h) = 20 $\text{mol}_{\text{Cy}} \text{mol}_{\text{Mo}}^{-1} \text{h}^{-1}$) [20]. The hybrid material $[\text{Mo}_2\text{O}_6(\text{trpzH})(\text{H}_2\text{O})_2]$ [trpzH = 4-(3,5-dimethyl-1H-pyrazol-4-yl)-1,2,4-triazole] was recently investigated as a catalyst under identical Cy reaction conditions, and led to a higher TOF (1 h) of 66 $\text{mol}_{\text{Cy}} \text{mol}_{\text{Mo}}^{-1} \text{h}^{-1}$ than **1** (20 $\text{mol}_{\text{Cy}} \text{mol}_{\text{Mo}}^{-1} \text{h}^{-1}$), but the former did not exhibit reaction-induced self-separating behavior [43]. For comparison, a commercial sample of MoO_3 (AnalaR, 99.5%) was tested

as catalyst instead of **1**, under similar reaction conditions. The epoxidation reaction with MoO_3 was slower (67% at 24 h) than with **1**, and furthermore the reaction mixture was always homogeneous and did not exhibit reaction-induced self-separating behavior.

The catalytic results for **2**/ H_2O_2 were compared with literature data for the hybrid material $[\text{WO}_3(2,2'\text{-bipy})] \cdot n\text{H}_2\text{O}$ ($n = 1\text{--}2$) and the oxodiperoxo complex $[\text{WO}_3(\text{O}_2)_2(2,2'\text{-bipy})]$ tested as catalysts under identical Cy reaction conditions [32]. The latter two tungsten compounds led to TON(24 h) = 98 $\text{mol}_{\text{Cy}} \text{mol}_{\text{Mo}}^{-1}$, which is slightly higher than that for **2**/ H_2O_2 [TON(24 h) = 85 $\text{mol}_{\text{Cy}} \text{mol}_{\text{Mo}}^{-1}$].

The superior catalytic results for (**1** or **2**)/ H_2O_2 over (**1** or **2**)/TBHP suggest that the two hybrid compounds are more efficient in activating H_2O_2 than TBHP. This is interesting since the conversion of H_2O_2 gives water as the coproduct, which is more eco-friendly than *tert*-butanol, the coproduct of TBHP conversion.

The higher catalytic activity of **1**/ H_2O_2 when compared with **2**/ H_2O_2 is somewhat unusual since molybdenum-based catalysts frequently display a lower activity than equivalent tungsten-based catalysts for olefin epoxidation in the presence of H_2O_2 . The situation is often reversed when TBHP is the oxidant, with the molybdenum-based catalysts being superior. Examples of compounds that exhibit this behavior (i.e., better catalytic results with Mo/TBHP and W/ H_2O_2) include the homogeneous catalysts $[\text{MO}_2\text{Cl}_2(\text{OPMePh}_2)_2]$ [44], $[\text{MO}_2\text{Cl}_2(\text{dppmO}_2)]$ (dppmO₂ = bis(diphenyl phosphineoxide)methane) [44], $[\text{Cp}^*_2\text{M}_2\text{O}_5]$ [45], and $[\text{MO}_2\text{L}]$ (L = diamine bis(phenolate) ligand) [46], oxodiperoxo complexes of the type $[\text{MO}(\text{O}_2)_2(\text{L})]$ supported on mesoporous SBA-15 materials [47], and the hybrid materials $[\text{MO}_3(2,2'\text{-bipy})] \cdot n\text{H}_2\text{O}$ ($n = 0\text{--}2$) [32]. As mentioned in the introduction, when aqueous H_2O_2 is used as the oxidant, the latter materials are converted to the partially soluble oxodiperoxo complexes $[\text{MO}(\text{O}_2)_2(2,2'\text{-bipy})]$, which are the active species responsible for the epoxidation reaction in homogeneous phase.

Computational studies have suggested that the reaction mechanism for Mo or W-catalyzed olefin epoxidation with H_2O_2 as oxidant involves the primary activation of the oxidant, where an oxo ligand (M=O) is protonated with concomitant formation of a hydroxide-hydroperoxo intermediate possessing the moiety $\{\text{M}(\text{OH})(\text{O}^\alpha\text{O}^\beta\text{H})\}$ [48–50]. Higher activity of W species is sometimes claimed and associated with a lower activation barrier for the rate-limiting step involving the transfer of the O^α atom to the olefin [48,50]. Specifically, natural bond orbital and natural population analysis studies suggested that the tungsten center may withdraw electron density from the σ bonding $[\text{O}^\alpha\text{O}^\beta]$ orbital more strongly than a molybdenum center, lowering the σ^* $[\text{O}^\alpha\text{O}^\beta]$ orbital energy and thus facilitating nucleophilic attack of the olefin. There is, however, added complexity since an alternative pathway exists involving external O^β transfer accompanied by a proton transfer from O^β to O^α , and the interaction strength between the W center and O^α may influence the O^β transfer process [49]. This pathway is not possible for an intermediate possessing the moiety $\{\text{M}(\text{OH})(\text{O}^\alpha\text{O}^\beta\text{tBu})\}$ formed in the case of TBHP. The operative oxygen transfer mechanism will clearly play a major role in determining the activities of Mo/W catalysts. On the other hand, an important factor which is sometimes discarded is the catalyst stability which may be influenced by the oxidizing conditions used.

In order to check whether compounds **1** and **2** possess catalase-type activity leading to non-productive decomposition of H_2O_2 (into O_2 and H_2O), iodometric titrations were carried out for the mixtures of (**1** or **2**)/ H_2O_2 /CH₃CN (without olefin) after stirring for 24 h at 70 °C. The H_2O_2 decomposition was ca. 90% for **1** and 60% for **2** (ca. 10% experimental error); the thermal decomposition of H_2O_2 (without catalyst and olefin) was negligible. These results indicate that compounds **1** and **2** possess catalase-type activity, which may explain the pressure relief observed upon opening

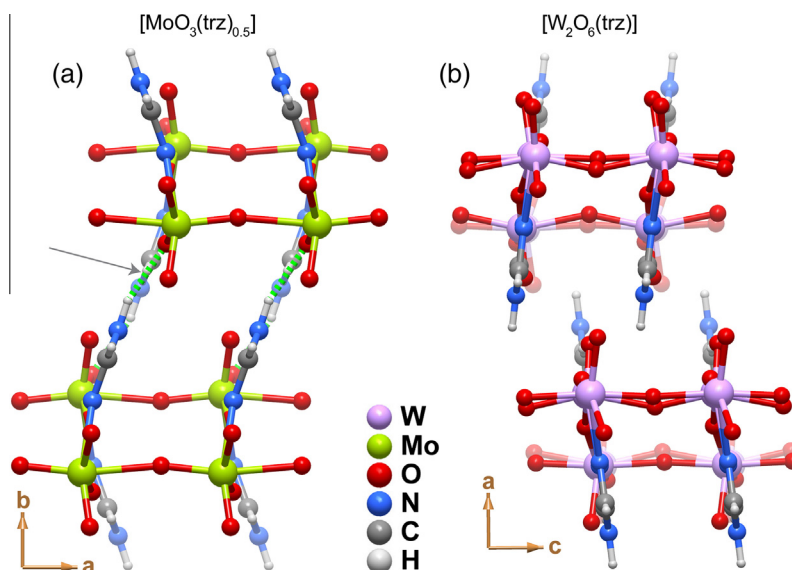


Fig. 5. Side view schematic representation of the mutual distribution of the 2D neutral $[\text{MoO}_3(\text{trz})_{0.5}]$ (a) and $[\text{W}_2\text{O}_6(\text{trz})]$ (b) layers present in compounds **1** and **2**, respectively. The dislocation of the layers on top of their growing planes leads to the loss of the strong and directional N–H...O interplanar hydrogen bonds (dashed green line indicated with an arrow) on going from **1** to **2**.

Table 3
Epoxidation of *cis*-cyclooctene with different oxidants in the presence of **1** or **2**.^a

Sample	Oxidant	Cy conversion (%) or TON ($\text{mol}_{\text{Cy}} \text{mol}_{\text{Mo}}^{-1}$) ^b
1	TBHP _{dec}	35
1	TBHP _{aq}	20
1 (run1)	H ₂ O ₂	98
1 /H ₂ O ₂ -run2	H ₂ O ₂	62
1 /H ₂ O ₂ -run3	H ₂ O ₂	59
2	TBHP _{dec}	9
2	TBHP _{aq}	3
2 (run1)	H ₂ O ₂	85
2 /H ₂ O ₂ -run2	H ₂ O ₂	81
2 /H ₂ O ₂ -run3	H ₂ O ₂	80

^a Initial mole ratios of metal:olefin:oxidant = 1:100:152, initial concentration of Cy = 1.2 M, 1 mL CH₃CN, 24 h reaction, 70 °C.

^b Cy conversion at 24 h reaction; the values of conversion coincide with those of turnover number (TON), at 24 h; CyO selectivity was always 100%.

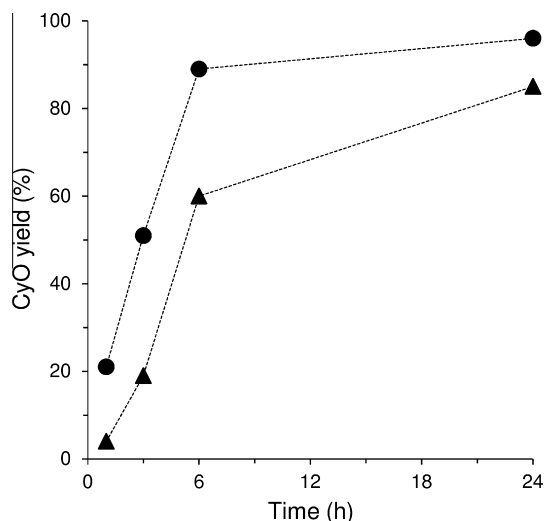


Fig. 6. *cis*-Cyclooctene epoxidation with H₂O₂ in the presence of **1** (●) or **2** (▲) at 70 °C (CH₃CN as cosolvent). The dashed lines are visual guides.

the reactors (after cooling to room temperature), i.e. the excess pressure was likely due to O₂ formed from the decomposition of H₂O₂. The final epoxide yield will depend at least partly on the relative rates of the Cy reaction (epoxidation activity) and H₂O₂ decomposition (catalase-type activity). The catalase-type activity may contribute to the slowdown of the reaction observed after 6 h, especially in the case of **1** (Fig. 6). Nevertheless, fairly high Cy conversions were reached after 24 h reaction (>85%).

3.3.2. Catalyst stability and formation of active species

For a typical batch run of Cy epoxidation at 70 °C with **1**/H₂O₂, the reaction mixture initially consisted of a white solid suspended in a colorless liquid phase, which after several minutes turned into a homogeneous transparent yellow solution (Fig. 7). After 24 h, the phase characteristics of the mixture had reverted back to that observed during the initial instants of the reaction, i.e. a white solid suspended in a colorless liquid phase. For **2**/H₂O₂ and the reactions performed with **1** or **2** and TBHP_{aq}/TBHP_{dec}, these phase transformations were never observed, i.e. the reaction mixtures always consisted of a white solid suspended in a colorless liquid phase.

For all reactions with **1** or **2** and the different oxidants, the reaction mixtures were centrifuged after 24 h in order to recover the solid phases. All of the recovered solids, which are referred to as **1**/oxidant-run1 and **2**/oxidant-run1 (oxidant = TBHP_{dec}, TBHP_{aq} or H₂O₂), exhibited FT-IR spectra and PXRD patterns that were similar to those of the corresponding original compounds **1** (Figs. 8 and 9) and **2** (Figs. S5 and S6 in the Supplementary Material). On the other hand, while SEM revealed an identical morphology for **2** and **2**/H₂O₂-run1, the morphologies for **1** and **1**/H₂O₂-run1 were strikingly different, changing from regular micro-sized parallelepipeds for **1** to aggregates of smaller irregular particles for **1**/H₂O₂-run1 (Fig. 3).

The solids **1**/H₂O₂-run1 and **2**/H₂O₂-run1 were reused for two consecutive 24 h batch runs (Table 3). For **1**, Cy conversion and epoxide yield decreased between runs 1 and 2, but then remained roughly constant at around 60%. For **2**, the catalytic performance was steady for the three runs (80–85% Cy conversion), which is consistent with the similar FT-IR spectra (Fig. S5), PXRD patterns (Fig. S6) and particle morphologies (Fig. 3) observed for as-synthesized **2** and the recovered solids.

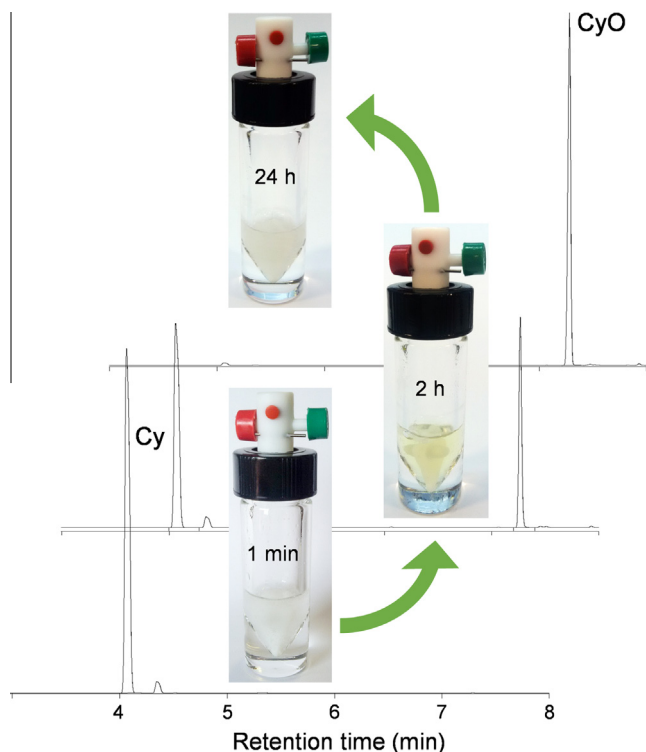


Fig. 7. Photographs and corresponding GC traces of the epoxidation of cyclooctene with aq. H_2O_2 at 70°C in the presence of **1** (CH_3CN as cosolvent): 1 min reaction, suspension of **1**; 2 h reaction, yellow homogeneous solution; 24 h reaction, compound **1** has precipitated.

The observation of a solid–liquid–solid phase transfer for the catalytic system **1**/ H_2O_2 /Cy/ CH_3CN / 70°C , together with the fact that as-synthesized **1** and **1**/ H_2O_2 -run*i* ($i = 1, 2, 3$) exhibited similar FT-IR spectra and PXRD patterns, suggest that during the catalytic reaction compound **1** is transformed into a different species (soluble and yellow in color) which, as the reaction approaches completion, is reversibly converted to a molybdenum oxide-triazole hybrid of the type **1**. This system therefore appears to exhibit the features required for a reaction-controlled solid–liquid–solid phase separation procedure. Several triazolylmolybdenum(VI) oxide hybrids recently investigated did not exhibit this behavior [43]. For example, the solid $[\text{Mo}_2\text{O}_6(\text{trpzH})(\text{H}_2\text{O})_2]$ (mentioned above) dissolved completely in the reaction mixture but did not self-precipitate [43].

Clearly, the type of oxidant influences the stability of **1**, and, on the other hand, H_2O_2 plays a role in the reversible formation of **1**. When **1** was mixed with Cy/ CH_3CN / H_2O (without H_2O_2), and stirred for 24 h at 70°C , no yellow coloring of the mixture was observed, and the FT-IR spectrum of the recovered solid (not shown here) matched that for **1**. Hence, while **1** is hydrolytically stable, in the presence of H_2O_2 it is transformed into a different compound. On the other hand, no reaction of Cy occurred for the Cy/ CH_3CN / H_2O mixture, indicating that H_2O_2 acts as oxygen atom-donor in the catalytic cycle. The reaction of Cy with H_2O_2 as limiting reagent (initial Cy: H_2O_2 mole ratio of 2.5) led to incomplete Cy reaction (Cy conversion at 24 h was 44% when based on the initial number of moles of Cy, and 100% when based on the initial number of moles of H_2O_2). For this experiment, a yellow colored liquid phase was initially obtained, but at 24 h the mixture consisted of a white solid suspended in a colorless liquid. These results suggest that compound **1** is reversibly formed upon the complete consumption of the oxidant. Furthermore, under the normal catalytic reaction conditions with a starting catalyst:olefin:ox-

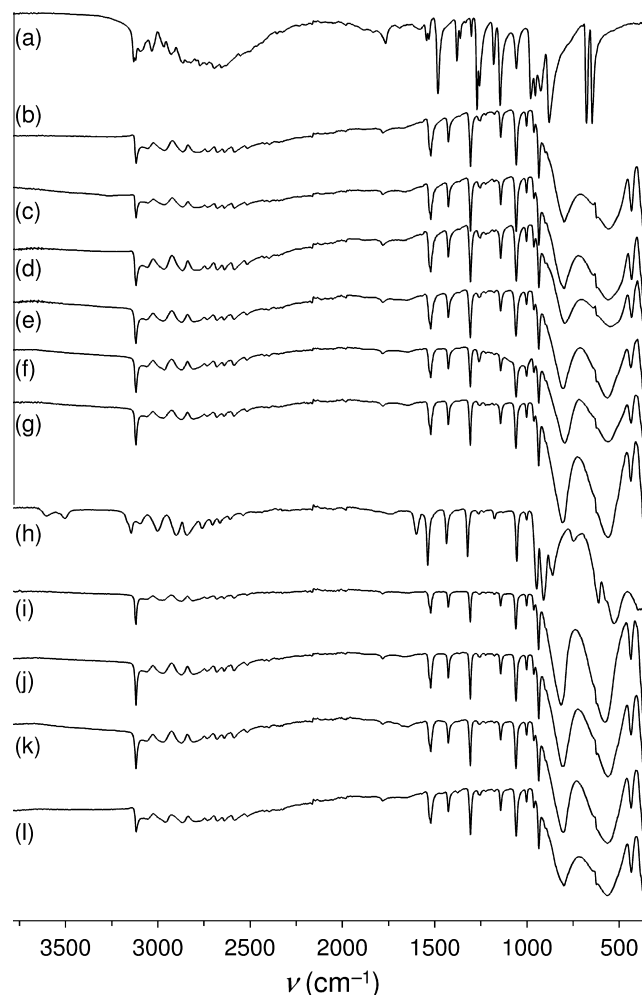


Fig. 8. ATR FT-IR spectra for the ligand 1,2,4-triazole (a), **1** (b) and the corresponding recovered solids **1**/TBHP_{dec}-run1 (c), **1**/TBHP_{aq}-run1 (d), **1**/ H_2O_2 -run1 (e), **1**/ H_2O_2 -run2 (f), **1**/ H_2O_2 -run3 (g), PS-(**1**-L-ct) (h), PS-(**1**-L-ct)-run1 (i), **1**-(methyl oleate)/ H_2O_2 (j), **1**-PhCH₂OH/ H_2O_2 (k), and **1**-PhMeS/ H_2O_2 (l).

idant mole ratio of 1:100:152, the catalase-type activity discussed above may contribute to the complete consumption of the oxidant.

To further understand the catalytic properties of **1** and **2**, a series of contact tests (without olefin) were performed. Compounds **1** or **2** were treated with oxidant (H_2O_2) and solvent (CH_3CN) for 24 h at 70°C . Subsequently, the resultant liquid (**1**-L-ct, **2**-L-ct) and solid (**2**-S-ct; no solid phase was present with **1**) phases were separated for further study. Catalytic tests with **1**-L-ct and **2**-L-ct (performed at 70°C after addition of the substrate Cy to the liquid phases) indicated negligible reaction of Cy. The solution **1**-L-ct was yellow in color, suggesting that it contained dissolved molybdenum species. The poor results for **1**-L-ct may therefore be due to the very low initial concentration of oxidant (according to the iodometric titrations). In the case of **2**-L-ct, the poor results of the catalytic test may be due to the absence of soluble active species (the solution was colorless), suggesting that the catalytic reaction with **2** is heterogeneous in nature. The catalytic test with **2**-S-ct gave similar results to those obtained with **2** (96% CyO selectivity at 85% conversion). These results are consistent with the similar FT-IR spectra (Fig. S5), PXRD patterns (Fig. S6), and particle morphologies (Fig. 3) of **2**-S-ct and **2**. Moreover, the 24 h batch run with **2**-S-ct led to a solid [(**2**-S-ct)-run1] which was recovered and found to exhibit similar FT-IR (Fig. S5) and PXRD (Fig. S6) data to those displayed by **2**. Hence, taking into account the similar

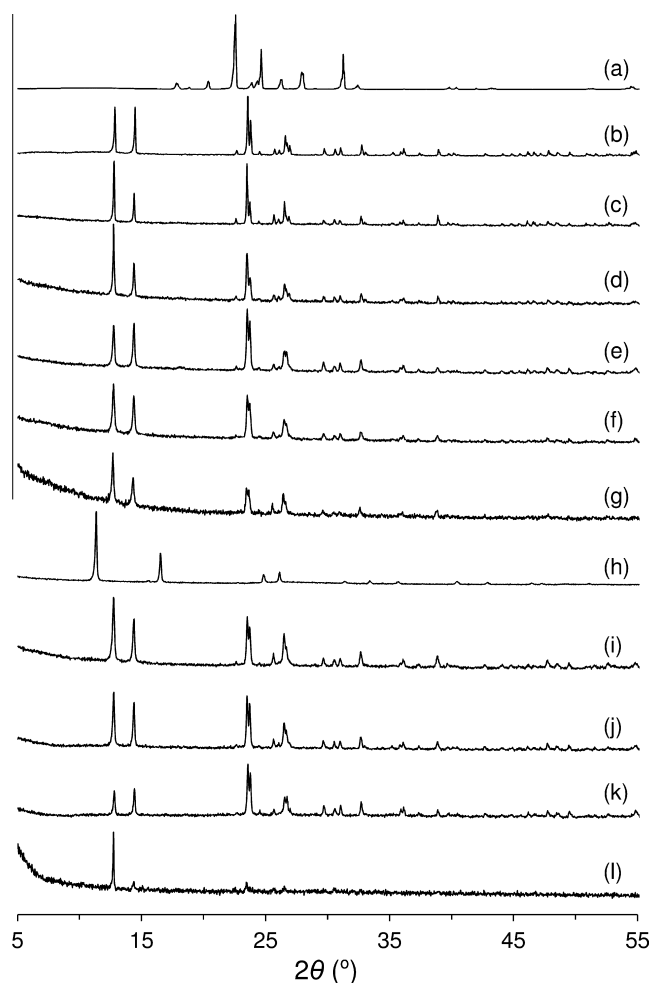


Fig. 9. PXRD patterns for the ligand 1,2,4-triazole (a), **1** (b) and the corresponding recovered solids **1**/TBHP_{dec}-run1 (c), **1**/TBHP_{aq}-run1 (d), **1**/H₂O₂-run1 (e), **1**/H₂O₂-run2 (f), **1**/H₂O₂-run3 (g), PS-(**1**-L-ct) (h), PS-(**1**-L-ct)-run1 (i), **1**-(methyl oleate)/H₂O₂ (j), **1**-PhCH₂OH/H₂O₂ (k), and **1**-PhMeS/H₂O₂ (l).

characterization data and steady catalytic performance of the solids reused in consecutive catalytic runs, compound **2** seems to behave as a fairly stable heterogeneous catalyst for Cy epoxidation with aq. H₂O₂.

A yellow solid [denoted PS-(**1**-L-ct)] was precipitated from the solution **1**-L-ct after concentrating the mixture by partial evaporation of the solvent at 70 °C. In comparison with **1**, the characterization data for PS-(**1**-L-ct) were different (Figs. 3, 8 and 9). In a catalytic test with PS-(**1**-L-ct), the solid completely dissolved and led to a Cy conversion of 69% at 24 h, with 100% CyO selectivity. Hence, the yellow compound possesses intrinsic activity as a homogeneous catalyst. The lower conversion reached for PS-(**1**-L-ct) in comparison with **1** (98% at 24 h, Table 3) may be partly due to differences in the initial molar concentration of catalyst since the catalytic tests were compared on the basis of the same initial mass of solid. As found for **1**, the catalytic test with PS-(**1**-L-ct) gave a yellow solution during the early stages of the reaction, but at 24 h the mixture had turned into a white solid suspended in a colorless liquid phase. FT-IR and PXRD data for the recovered solid [PS-(**1**-L-ct)-run1] were similar to those for **1** (Figs. 8 and 9). These results support the hypothesis that **1** is reversibly converted into a different (yellow colored, soluble) compound during the catalytic reaction. The reversibility of this process may partly explain why **1** undergoes morphological changes during the catalytic reaction, despite the retention of the chemical and crys-

talline structural features (discussed above). Specifically, the reversible transformation of **1** during the catalytic reaction seems to be accompanied by a reduction in the average particle size (Fig. 3).

As noted above, the FT-IR spectrum of PS-(**1**-L-ct) is clearly distinct from that for **1**, showing differences in both the ligand modes and the Mo–O bands (Fig. 8). New, weak bands are present at 3505 and 3600 cm⁻¹, possibly due to N–H and/or O–H stretching vibrations (the latter may arise from coordinating or crystallization molecules of water). A comparison of the spectra for **1** and PS-(**1**-L-ct) in the 1000–1550 cm⁻¹ range confirms that the organic ligand is retained in the yellow species isolated from the contact test, although some of the bands are shifted by up to 17 cm⁻¹ when compared with the corresponding bands for **1**. A new medium intensity band at 1599 cm⁻¹ for PS-(**1**-L-ct) may be due to ν (C=N) of triazole or, possibly, an N–H or water bending vibration (if weakly hydrogen-bonded). Below 1000 cm⁻¹, the IR spectrum of PS-(**1**-L-ct) displays two strong bands at 910 and 947 cm⁻¹, which may both be due to ν (Mo=O) (cf. 937 cm⁻¹ for **1**). The disruption of the 2D network structure of **1** to give PS-(**1**-L-ct) is evident from the disappearance of the very strong, broad ν (Mo–O–Mo) bands at 595 and 842 cm⁻¹. Instead, PS-(**1**-L-ct) exhibits a medium-strong band at 860 cm⁻¹ and a very strong band at 528 cm⁻¹, which are attributed to ν (Mo–O)_{peroxo} and ν (O–O) vibrations, respectively. Hence, PS-(**1**-L-ct) is most likely a mononuclear or polynuclear oxo-peroxo molybdenum species. Although PS-(**1**-L-ct) may be indicative of the type of active species present in solution under the normal catalytic reaction conditions, the actual species present may fluctuate according to changes in the composition of the reaction mixture caused by consumption of the oxidant and conversion of Cy to CyO. This was evident when performing the contact test with shorter reaction times (less than 24 h), which typically led to the isolation of species with FT-IR spectra different from that for PS-(**1**-L-ct).

The behavior of **1** in liquid-phase catalytic olefin epoxidation parallels that recently reported for octamolybdate-based self-separating catalysts of general formula [cation]₄Mo₈O₂₆ (cation = 1-hexyl-3-methylimidazolium, 1,2-dimethyl-3-hexylimidazolium, or 1-hexylpyridinium) [20]. Thus, with Cy as substrate, the octamolybdate salts dissolved in the presence of H₂O₂ and CH₃CN to give yellow homogeneous solutions, possibly containing oxodiperoxomolybdenum active species. As found for **1**, self-precipitation of the starting octamolybdate salts took place after the completion of reaction took place. Several mechanistic hypotheses have been put forward in the literature (mainly based on gas-phase density functional theory) for olefin epoxidation with hydroperoxides in the presence of oxoperoxomolybdenum species; reaction mechanisms may involve O-atom transfer from a η^2 -O₂ peroxo ligand [51–53] or a hydroperoxo (or alkylperoxo) ligand [52,54,55] to the olefin (which may or may not be coordinated to the metal center).

3.3.3. Catalytic performance with different substrates

The liquid-phase oxidation of benzyl alcohol (PhCH₂OH) to benzaldehyde (PhCHO) is an important reaction since PhCHO is commonly used as a food flavorant, perfume ingredient, industrial solvent, and as an intermediate in the synthesis of other organic compounds, such as pharmaceuticals, plastic additives, and aniline dyes [56]. Further oxidation of PhCHO gives benzoic acid (PhCO₂H), which is used as a preservative in food, drugs, and personal care products, and as an intermediate in the synthesis of various chemicals such as ϵ -caprolactam and terephthalic acid [57]. The value of PhCHO and PhCO₂H has motivated the development of catalytic systems for the oxidation of PhCH₂OH with aq. H₂O₂ [58,59].

The catalytic performances of **1** and **2** were explored for the oxidation of PhCH₂OH and PhCHO with H₂O₂ at 70 °C. The reaction of

PhCH₂OH gave PhCHO and PhCO₂H, which were formed with a total selectivity of 100% (Fig. 10). The dependence of product selectivity on PhCH₂OH conversion was roughly comparable for **1** and **2**, until ca. 75% conversion. Initially, PhCHO was the only product (100% selectivity at 10–11% conversion), and subsequently PhCHO selectivity decreased with the concomitant increase of PhCO₂H selectivity, leading to 45% PhCHO and 30% PhCO₂H yield for **1**, and 40% PhCHO and 56% PhCO₂H yield for **2**, at 48 h. These results are consistent with the conversion of PhCH₂OH to PhCO₂H via the intermediate formation of PhCHO. The oxidation of PhCHO (as substrate) with H₂O₂, in the presence of **1** or **2** at 70 °C, gave PhCO₂H as the only product (80% and 72% yield, respectively, at 24 h reaction, Fig. 11). While for the reaction of PhCH₂OH, **2** led to higher conversions than **1** (96% and 75% conversion, respectively, at 48 h reaction), the opposite was observed for the reaction of PhCHO (80% and 72% conversion for **1** and **2**, respectively, at 24 h). These results may be due to different reaction mechanisms involved and/or different rates of substrate oxidation relative to H₂O₂ decomposition.

The **1**/H₂O₂ system was further investigated for the conversion of cyclohexene and *trans*-2-octene, and the biomass-derived olefins DL-limonene and methyl oleate, at 70 °C (Table 4). In general, the corresponding epoxide was formed, as well as the diol product via hydrolysis of the oxirane ring, e.g. 59% cyclohexane-1,2-diol selectivity at 90% cyclohexene oxide conversion, and 56% limonene-1,2-diol selectivity at 55% limonene conversion. Hence, the **1**/H₂O₂ system promotes one-pot epoxidation and hydrolysis reactions for olefins which give relatively reactive epoxides. Side-reactions included allylic oxidation of C–H bonds to give alcohol and carbonyl products, e.g. cyclohex-2-en-1-ol and cyclohex-2-en-1-one were formed from cyclohexene, and 2-methyl-5-(prop-1-en-2-yl)cyclohex-2-en-1-ol (carveol) and 2-methyl-5-(prop-1-en-2-yl)cyclohex-2-en-1-one (carvone) were formed from DL-limonene. The ability of the **1**/H₂O₂ system to convert alcohols to the corresponding carbonyls is consistent with its ability to oxidize PhCH₂OH to PhCHO.

The catalytic versatility of the **1**/H₂O₂ system was explored for the oxidation of sulfides into sulfoxides or sulfones (Table 4). This transformation has received much interest in the context of processes for the oxidative desulfurization of liquid fuels [60]. Moreover, sulfoxides and sulfones are versatile intermediates in organic synthesis [61]. The reaction of methylphenylsulfide (PhMeS) with H₂O₂ in the presence of **1** led to 99% conversion at 6 h, and gave the corresponding sulfoxide and sulfone with 39% and 61% selectivity, respectively. With benzothiophene (BzS), the sulfone (1-benzothiophene 1,1-dioxide) was formed with 100% selectivity at 72% conversion (24 h). The conversion of the substrates to the corresponding sulfones involves the intermediate formation of the sulfoxide [61]. For the two substrates, no oxidation of the phenyl C–H bonds was observed.

There are few reports that describe the use of molybdenum oxide-organic hybrids or oxoperoxo compounds as (pre)catalysts for the oxidation of PhMeS and BzS with aqueous H₂O₂ [62–66]. Organotin molybdates of the type [(R₃Sn)₂MoO₄]_nH₂O (R = methyl, *n*-butyl, cyclohexyl, phenyl, benzyl) were tested as catalysts for the BzS reaction with H₂O₂ at 35 °C (Mo:substrate:H₂O₂ = 1:100:200) [62]. With CH₃CN as solvent and the benzyl derivative as catalyst, the corresponding sulfone was formed with ca. 100% selectivity at 65% conversion (7 h). The oxodiperoxo complex [MoO(O₂)₂(3-methylpyrazole)] was tested as catalyst for the reactions of PhMeS and BzS in an ionic liquid medium at 20 °C (Mo:substrate:H₂O₂ = 1:40:40) [63]. With PhMeS as substrate, the corresponding sulfoxide was formed with 96% selectivity at 80% conversion (1 h), while with BzS as substrate the sulfoxide was formed with 1% selectivity at 65% conversion, with no formation of sulfone being reported. A molybdenum based metallomicellar catalyst, (C₁₉H₄₂N)₂[MoO(O₂)₂(C₂O₄)]₂·H₂O, was tested with PhMeS

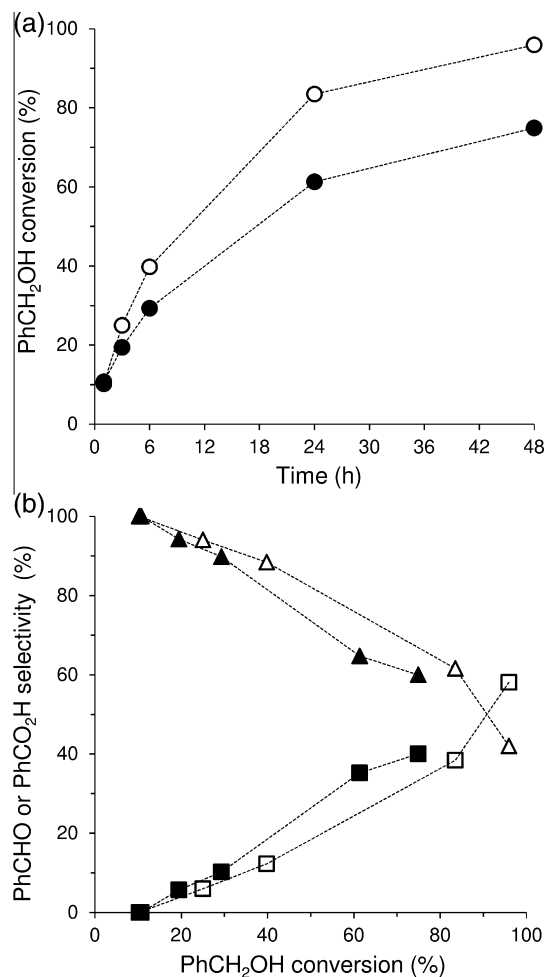


Fig. 10. (A) Conversion of benzyl alcohol (●, ○) and (B) selectivity to benzaldehyde (▲, △) and benzoic acid (■, □) for the reaction of benzyl alcohol with H₂O₂ in the presence of **1** (filled symbols) or **2** (open symbols) at 70 °C. The dashed lines are visual guides.

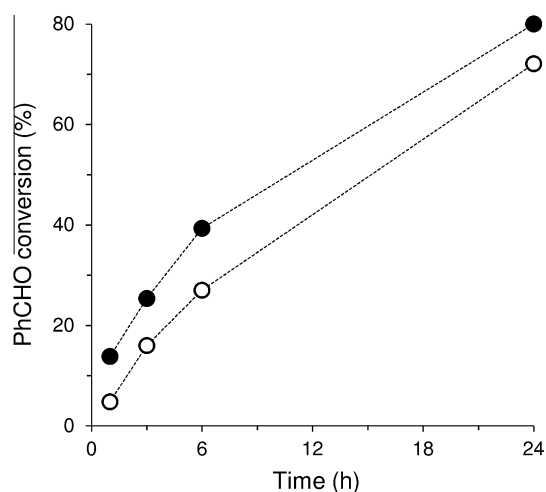
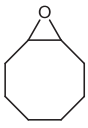
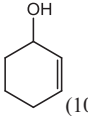
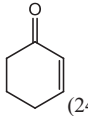
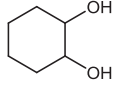
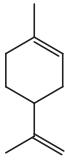
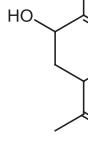
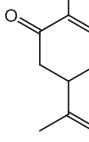
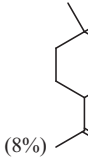
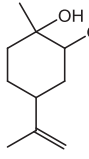
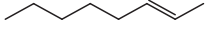
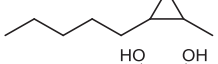
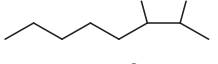
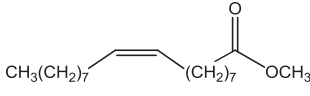
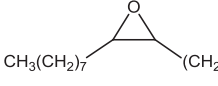
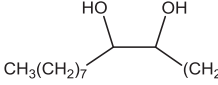
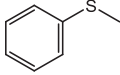
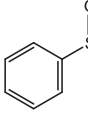
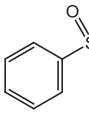
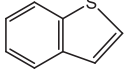
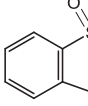


Fig. 11. Reaction of benzaldehyde with H₂O₂ in the presence of **1** (●) or **2** (○) at 70 °C. Selectivity to benzoic acid was always 100%. The dashed lines are visual guides.

as substrate at room temperature, leading to 95% sulfoxide yield at 30 min (Mo:substrate:H₂O₂ = 1:40:40); increasing the amount of oxidant (Mo:substrate:H₂O₂ = 1:40:120) promoted the formation

Table 4
Conversion of different substrates using **1**/H₂O₂.^a

Substrate	Conv. (%) ^b	Product selectivities (%) ^c
 cis-cyclooctene	98	 (100)
 cyclohexene	90	 (10%)  (24%)  (59%)
 DL-Limonene	55	 (4%)  (12%)  (8%)  (56%)
 trans-2-octene	42	 (9%)  (31%)
 methyl oleate	39	 (50%)  (10%)
 methylphenylsulfide	99 ^d	 (39%)  (61%)
 benzothiophene	72	 (100%)

^a Initial Mo:substrate:H₂O₂ molar ratio = 1:100:152, initial concentration of substrate = 1.2 M, 1 mL CH₃CN, 70 °C.

^b Substrate conversion at 24 h reaction (unless otherwise specified).

^c Product selectivity indicated in parentheses; for the substrates cyclohexene and limonene, epoxide was formed in less than 1% yield; other products were formed which were not clearly identified.

^d Reaction time of 6 h.

of the sulfone (97% yield at 10 min) [64]. In a different approach, and somewhat in parallel with that observed for **1**/H₂O₂, peroxomolybdenum species may be formed in situ from pre-catalysts, promoting sulfoxidation reactions with H₂O₂ [65,66]. For example, *cis*-[Mo(CO)₄(eppa)] {eppa = ethyl[3-(2-pyridyl)-1-pyrazolyl]acetate} was converted to [MoO(O₂)₂(eppa)] in situ during PhMeS reaction at 35 °C, leading to 100% sulfoxide selectivity at 88% conversion (Mo:substrate:H₂O₂ = 1:40:40; 6 h) [65]. For **1**/H₂O₂, using a Mo:substrate:H₂O₂ molar ratio of 1:100:152 and higher reaction temperature of 70 °C shifted the sulfide-to-sulfoxide-to-sulfone cascade reaction system toward the formation of the end product (61% sulfone yield at 99% conversion, 6 h). When the reaction temperature was decreased from 70 to 35 °C and the amount of oxidant was decreased (Mo:substrate:H₂O₂ = 1:40:40), the catalytic system **1**/H₂O₂ led to 99% PhMeS conversion at 6 h, and the

corresponding sulfoxide and sulfone products were formed with 89% and 11% selectivity. Hence, under similar conditions to those used for [MoO(O₂)₂(eppa)] [65], the PhMeS reaction was faster for **1**, promoting the formation of the sulfoxide.

3.3.4. Catalyst behavior and recovery with different substrates

With PhCH₂OH as substrate and **1** or **2** as (pre)catalyst, the catalyst behavior (solid-liquid-solid phase transfer vs. heterogeneous) paralleled that observed for **1** and **2** in the reaction of Cy. Accordingly, the FT-IR spectra and PXRD patterns of the original and recovered solids were similar (Figs. 8 and 9 for **1**, and Figs. S5 and S6 in the Supplementary Material for **2**). The reaction-induced self-separating behavior was also observed for the **1**/H₂O₂ system and other olefin/sulfide substrates; Figs. 8 and 9 show representative FT-IR and PXRD data for the solids recovered

from the **1**-(methyl oleate)/H₂O₂ and **1**-PhMeS/H₂O₂ systems. For the latter, the intermediate formation of metal species of the type PS-(**1**-L-ct) (as isolated in the **1**-Cy/H₂O₂ system) was confirmed by precipitating a yellow solid from the liquid phase; the FT-IR spectrum of this solid was similar to that for PS-(**1**-L-ct).

4. Conclusions

In this work the tungsten analogue of the known molybdenum oxide-triazole hybrid material [MoO₃(trz)_{0.5}] has been successfully prepared by hydrothermal synthesis. Under the reaction conditions used, the W and Mo phases were obtained as microcrystalline powders. Therefore, the solid-state structures were determined by Rietveld analysis of high-resolution powder X-ray diffraction data, supported by spectroscopic data (¹H and ¹³C CP MAS NMR, and FT-IR). The structure for [MoO₃(trz)_{0.5}] (**1**) is identical to that previously found by single-crystal X-ray diffraction [26]. The W phase (**2**) has a different space group, but displays the same type of undulating two-dimensional (2D) metal oxide network structure. Compounds **1** and **2** have been shown to display distinct catalytic behaviors with aqueous H₂O₂ as oxidant. Whereas the hybrid **2** behaves as a fairly stable heterogeneous catalyst, the hybrid **1** displays reaction-controlled phase-transfer (solid-liquid-solid) behavior, and thus it can be used as a self-separating catalyst. The self-separating behavior of **1**/H₂O₂ was observed with different substrates and reaction systems. To the best of our knowledge, the hybrid **1** is the first example of a self-precipitating catalyst that has an extended 1D, 2D or 3D crystalline structure. The reasons why **1** displays this unprecedented behavior are not yet fully understood, but possible factors include the structure-directing influence of the ligand trz, which leads to unique structures for **1** and (presumably) the active species present in solution, and the dual epoxidation and catalase-like activities. We plan to investigate other types of metal oxide-triazole hybrid materials in anticipation of finding new examples of phase transfer catalysts that combine the advantages of homogeneous and heterogeneous catalysts.

Acknowledgments

We acknowledge funding by FEDER (Fundo Europeu de Desenvolvimento Regional) through COMPETE (Programa Operacional Factores de Competitividade). National funding through the FCT (Fundação para a Ciência e a Tecnologia) within the projects FCOMP-01-0124-FEDER-029779 (FCT ref. PTDC/QEQ-SUP/1906/2012) and FCOMP-01-0124-FEDER-041282 (FCT ref. EXPL/CTM-NAN/0013/2013) is thanked. This work was developed in the scope of the project CICECO – Aveiro Institute of Materials, POCI-01-0145-FEDER-007679 (FCT ref. UID/CTM/50011/2013), financed by national funds through the FCT/MEC and co-financed by FEDER under the PT2020 Partnership Agreement. The FCT and the European Union are acknowledged for postdoctoral grants to P.N. (SFRH/BPD/73540/2010) and T.R.A. (SFRH/BPD/97660/2013) cofunded by MCTES and the European Social Fund through the program POPH of QREN. The authors are grateful to the ESRF (Grenoble, France) for approving the experiment CH-4254 (ID22).

Appendix A. Supplementary material

CIF files for **1** and **2**, additional characterization data for **1** and **2** (TGA curves, FT-IR spectra, solid-state ¹³C and ¹H MAS NMR spectra), and for the solids recovered after the contact tests and catalytic runs using **2** (ATR FT-IR spectra and PXRD patterns). Supplementary data associated with this article can be found, in the online version, at <http://dx.doi.org/10.1016/j.jcat.2016.06.005>.

References

- [1] W.A. Herrmann, B. Cornils, *Angew. Chem., Int. Ed. Engl.* 36 (1997) 1048–1067.
- [2] D.J. Cole-Hamilton, *Science* 299 (2003) 1702–1706.
- [3] P. McMorn, G.J. Hutchings, *Chem. Soc. Rev.* 33 (2004) 108–122.
- [4] A. Corma, H. Garcia, *Adv. Synth. Catal.* 348 (2006) 1391–1412.
- [5] K.R. Jain, F.E. Kühn, *Dalton Trans.* (2008) 2221–2227.
- [6] S. Shylesh, M. Jia, W.R. Thiel, *Eur. J. Inorg. Chem.* (2010) 4395–4410.
- [7] Z. Xi, N. Zhou, Y. Sun, K. Li, *Science* 292 (2001) 1139–1141.
- [8] V.K. Dioumaev, R.M. Bullock, *Nature* 424 (2003) 530–532.
- [9] M. Süßner, H. Plenio, *Angew. Chem., Int. Ed.* 44 (2005) 6885–6888.
- [10] X. Yang, S. Gao, Z. Xi, *Org. Proc. Res. Dev.* 9 (2005) 294–296.
- [11] H. Chen, W.-L. Dai, X.-L. Yang, R. Gao, Y. Cao, H. Li, K. Fan, *Appl. Catal. A: Gen.* 309 (2006) 62–69.
- [12] Z. Weng, G. Liao, J. Wang, X. Jian, *Catal. Commun.* 8 (2007) 1493–1496.
- [13] Z. Weng, J. Wang, X. Jian, *Catal. Commun.* 9 (2008) 1688–1691.
- [14] Y. Ding, W. Zhao, H. Hua, B. Ma, *Green Chem.* 10 (2008) 910–913.
- [15] B. Ma, W. Zhao, F. Zhang, Y. Zhang, S. Wu, Y. Ding, *RSC Adv.* 4 (2014) 32054–32062.
- [16] Y. Qiao, Z. Hou, H. Li, Y. Hu, B. Feng, X. Wang, L. Hua, Q. Huang, *Green Chem.* 11 (2009) 1955–1960.
- [17] Y. Leng, J. Wang, D. Zhu, X. Ren, H. Ge, L. Shen, *Angew. Chem., Int. Ed.* 48 (2009) 168–171.
- [18] P. Zhao, J. Wang, G. Chen, Y. Zhou, J. Huang, *Catal. Sci. Technol.* 3 (2013) 1394–1404.
- [19] Y. Chen, R. Tan, W. Zheng, Y. Zhang, G. Zhao, D. Yin, *Catal. Sci. Technol.* 4 (2014) 4084–4092.
- [20] M.-D. Zhou, M.-J. Liu, L.-L. Huang, J. Zhang, J.-Y. Wang, X.-B. Li, F.E. Kühn, S.-L. Zang, *Green Chem.* 17 (2015) 1186–1193.
- [21] Y. Ding, W. Zhao, *J. Mol. Catal. A: Chem.* 337 (2011) 45–51.
- [22] W. Zhao, C. Yang, Y. Ding, B. Ma, *New J. Chem.* 37 (2013) 2614–2618.
- [23] K. Li, L. Chen, H. Wang, W. Lin, Z. Yan, *Appl. Catal. A: Gen.* 392 (2011) 233–237.
- [24] D. Liu, J. Gui, F. Ju, Z. Sun, Y.-K. Park, *Catal. Lett.* 142 (2012) 1330–1335.
- [25] Y. Zhou, Z. Guo, W. Hou, Q. Wang, J. Wang, *Catal. Sci. Technol.* 5 (2015) 4324–4335.
- [26] P.J. Hagrman, R.L. LaDuca Jr., H.-J. Koo, R. Rarig Jr., R.C. Haushalter, M.-H. Whangbo, J. Zubieta, *Inorg. Chem.* 39 (2000) 4311–4317.
- [27] M. Abrantes, T.R. Amarante, M.M. Antunes, S. Gago, F.A.A. Paz, I. Margiolaki, A. E. Rodrigues, M. Pillinger, A.A. Valente, I.S. Gonçalves, *Inorg. Chem.* 49 (2010) 6865–6873.
- [28] M. Abrantes, I.S. Gonçalves, M. Pillinger, C. Vurchio, F.M. Cordero, A. Brandi, *Tetrahedron Lett.* 52 (2011) 7079–7082.
- [29] T.R. Amarante, P. Neves, A.A. Valente, F.A.A. Paz, A.N. Fitch, M. Pillinger, I.S. Gonçalves, *Inorg. Chem.* 52 (2013) 4618–4628.
- [30] T.R. Amarante, P. Neves, F.A.A. Paz, A.A. Valente, M. Pillinger, I.S. Gonçalves, *Dalton Trans.* 43 (2014) 6059–6069.
- [31] T.R. Amarante, P. Neves, A.C. Gomes, M.M. Nolasco, P. Ribeiro-Claro, A.C. Coelho, A.A. Valente, F.A.A. Paz, S. Smeets, L.B. McCusker, M. Pillinger, I.S. Gonçalves, *Inorg. Chem.* 53 (2014) 2652–2665.
- [32] T.R. Amarante, M.M. Antunes, A.A. Valente, F.A.A. Paz, M. Pillinger, I.S. Gonçalves, *Inorg. Chem.* 54 (2015) 9690–9703.
- [33] A.N. Fitch, *J. Res. Natl. Inst. Stand. Technol.* 109 (2004) 133–142.
- [34] A. Coelho, Topas Academic, Version 5.0, Coelho Software, Brisbane, 2013.
- [35] A. Coelho, *J. Appl. Crystallogr.* 36 (2003) 86–95.
- [36] R.W. Cheary, A.A. Coelho, *J. Appl. Crystallogr.* 25 (1992) 109–121.
- [37] F. Billes, H. Endrédi, G. Keresztury, *J. Mol. Struct. (Theochem)* 530 (2000) 183–200.
- [38] D. Bougeard, N.L. Calvé, B.S. Roch, A. Novak, *J. Chem. Phys.* 64 (1976) 5152–5164.
- [39] J.G. Haasnoot, G. Vos, W.L. Groeneveld, *Z. Naturforsch. B* 32 (1977) 1421–1430.
- [40] W.H. Baur, *Acta Crystallogr., Sect. B: Struct. Sci.* 30 (1974) 1195–1215.
- [41] As detailed in Sections 2.4 and 3.2, the high-resolution synchrotron PXRD studies indicated the presence of trace amounts of unidentified crystalline impurities in the as-synthesised samples for **1** and **2** (not detectable through standard in-house PXRD measurements). Although we cannot exclude the possibility that these impurities could be catalytically active in the reaction systems studied, we consider it reasonable to discount any possible catalytic contribution due to the very low amounts present (<1%).
- [42] C.A. Gamelas, A.C. Gomes, S.M. Bruno, F.A.A. Paz, A.A. Valente, M. Pillinger, C.C. Romão, I.S. Gonçalves, *Dalton Trans.* 41 (2012) 3474–3484.
- [43] A.B. Lysenko, G.A. Senchyk, K.V. Domasevitch, J. Hauser, D. Fuhrmann, M. Kobalz, H. Krautscheid, P. Neves, A.A. Valente, I.S. Gonçalves, *Inorg. Chem.* 54 (2015) 8327–8338.
- [44] A. Jimtaisong, R.L. Luck, *Inorg. Chem.* 45 (2006) 10391–10402.
- [45] P. Sözen-Aktaş, E. Manoury, F. Demirhan, R. Poli, *Eur. J. Inorg. Chem.* (2013) 2728–2735.
- [46] F. Madeira, S. Barroso, S. Namorado, P.M. Reis, B. Royo, A.M. Martins, *Inorg. Chim. Acta* 383 (2012) 152–156.
- [47] J. Tang, L. Wang, G. Liu, Y. Hou, W. Zhang, M. Jia, W.R. Thiel, *J. Mol. Catal. A: Chem.* 313 (2009) 31–37.
- [48] C. Dinol, M. Ciclosi, E. Manoury, L. Maron, L. Perrin, R. Poli, *Chem. Eur. J.* 16 (2010) 9572–9584.
- [49] C. Dinol, R. Poli, L. Perrin, L. Maron, *Dalton Trans.* 41 (2012) 1131–1133.
- [50] A. Comas-Vives, A. Lledós, R. Poli, *Chem. Eur. J.* 16 (2010) 2147–2158.
- [51] M. Herbert, E. Álvarez, D.J. Cole-Hamilton, F. Montilla, A. Galindo, *Chem. Commun.* 46 (2010) 5933–5935.

- [52] V. Yudanov, *J. Struct. Chem. Suppl.* 48 (2007) S111–S124.
- [53] M. Drees, S.A. Hauser, M. Cokoja, F.E. Kühn, *J. Organomet. Chem.* 748 (2013) 36–45.
- [54] M. Herbert, F. Montilla, E. Álvarez, A. Galindo, *Dalton Trans.* 41 (2012) 6942–6956.
- [55] M.J. Calhorda, P.J. Costa, *Curr. Org. Chem.* 16 (2012) 65–72.
- [56] R.V. Sharma, K.K. Soni, A.K. Dalai, *Catal. Commun.* 29 (2012) 87–91.
- [57] E. Arceo, J.A. Ellman, R.G.A. Bergman, *ChemSusChem* 3 (2010) 811–813.
- [58] G. Ming-Lin, L. Hui-Zhen, *Green Chem.* 9 (2007) 421–423.
- [59] S. Xiao, C. Zhang, R. Chen, F. Chen, *New J. Chem.* 39 (2015) 4924–4932.
- [60] V.C. Srivastava, *RSC Adv.* 2 (2012) 759–783.
- [61] S. Caron, R.W. Dugger, S.G. Ruggeri, J.A. Ragan, D.H.B. Ripin, *Chem. Rev.* 106 (2006) 2943–2989.
- [62] M. Abrantes, A.A. Valente, M. Pillinger, I.S. Gonçalves, J. Rocha, C.C. Romão, *Chem. Eur. J.* 9 (2003) 2685–2695.
- [63] C.J. Carrasco, F. Montilla, E. Álvarez, C. Mealli, G. Manca, A. Galindo, *Dalton Trans.* 43 (2014) 13711–13730.
- [64] R.D. Chakravarthy, V. Ramkumar, D.K. Chand, *Green Chem.* 16 (2014) 2190–2196.
- [65] P. Neves, T.R. Amarante, A.C. Gomes, A.C. Coelho, S. Gago, M. Pillinger, I.S. Gonçalves, C.M. Silva, A.A. Valente, *Appl. Catal. A: Gen.* 395 (2011) 71–77.
- [66] L.F. Veiros, C.A. Gamelas, M.J. Calhorda, C.C. Romão, *Organometallics* 30 (2011) 1454–1465.